Capillary pinching in a pinched microchannel

O. Amyot and F. Plouraboué

Citation: Phys. Fluids **19**, 033101 (2007); doi: 10.1063/1.2709704
View online: http://dx.doi.org/10.1063/1.2709704
View Table of Contents: http://pof.aip.org/resource/1/PHFLE6/v19/i3
Published by the American Institute of Physics.

Capillary pinching in a pinched microchannel

O. Amyot and F. Plouraboué
Institut de Mécanique des Fluides de Toulouse, UMR CNRS-INPT/UPS No. 5502, Avenue du Professeur Camille Soula, 31400 Toulouse, France

(Received 13 April 2006; accepted 17 January 2007; published online 14 March 2007)

We report a study of the capillary pinching of a gas bubble by a wetting liquid inside a pinched channel. The capillary pinching induces very reproducible bubbling, at a very well-defined frequency. There are two regimes associated with drip and jet bubbling. In the latter, we show that highly monodispersed bubbles are formed by our pinched channel. The dynamics of the bubble formation also shows two distinct regimes: a long-duration elongation of the air bubble and a rapid relaxation of the interface after interface breakup. The slow regime depends on the flux imposed and the channel geometry. The rapid deformation dynamic regime depends very weakly on the boundary conditions. Scaling arguments are proposed in the context of the lubrication approximation to describe the two regimes. © *2007 American Institute of Physics*. [DOI: 10.1063/1.2709704]

I. INTRODUCTION

Capillary breakup in open flows is mainly controlled by flow field strain deformation and capillary forces. The particular interface dynamics near the pinch-off has been thoroughly investigated[1–3] in the case of liquid jets in open air. Moreover, in the case of open coaxial gas-liquid flows, two main flow configurations have been described: dripping and jetting modes (see, for example, Refs. 4 and 6). In such works, the transition between the dripping and the jetting regime is described and analyzed in the framework of linear stability analysis.[4,6] The onset of the dripping-jetting transition has been associated with the absolute-convective instability of a gas jet in a coflowing liquid by Sevilla *et al.*[4] when considering a nearly inviscid flow, and by Gañán-Calvo *et al.*[6] in a more general frame covering a wide range of Reynolds and Weber numbers. Furthermore, in a similar context, Gañán-Calvo *et al.*[7] have studied the properties of bubble formation in an open jet coming out of a flow focusing injector. Their experimental results and new experimental observations have been collapsed into a simple scaling law,[8] which takes the dominant effects of inertia in the fluid surrounding the gas into account.

Beside open coaxial flows, there is a growing interest in flow breakup in confined channels for microfluidic applications. There is indeed considerable motivation to better understand how suitable injectors could monitor the encapsulation process. When confined two-phase flows are considered, both the main flow field characteristics and the capillary pinch-off are principally controlled by the channel shape, although different flow regimes can be observed when the flow parameters are varied.[9,10] In the context of microfluidics, a better control of encapsulated phases could be used for separation and/or aggregation purposes.[5] Highly uniform emulsion droplets can be formed by focusing flow through small holes,[11–14] micromachined combs,[15] or T-shaped junctions.[10] Such encapsulation can be obtained from the building and design of injector structures, where one phase continuously flows into another one.[10,12–14,16] Again, in this context, two main mechanisms for the emulsification in coaxial flows have been described: dripping or jetting modes. The dripping mode is associated with drops produced at the entrance of the collection tube, which generates highly monodispersed emulsion in which the drop diameter is very close to the radius of the injector orifice. In contrast, jetting is referred to as "quite irregular, resulting in polydisperse droplets whose radii are much greater than that of the jet." The diameter of the drops reported in Ref. 14 for the jetting mode are within a factor of 2 of that of the injector orifice. It is interesting to note that the jetting regime described in Refs. 13 and 14 is viscous dominated as opposed to previous other inertia dominated jetting (e.g., Ref. 7), whereas intermediate situations have also been considered.[12] Hence, for the injector types proposed in Ref. 14, the best way to change the drop diameter is to change the injector orifice. As pointed out by Link *et al.*,[10] reducing polydispersity in drop generation can be an important issue in many applications. On the other hand, it will be very interesting to find versatile devices that could generate monodispersed droplets having different sizes depending on flow parameters, such as those proposed in Refs. 7 and 12. In this paper, we report on the behavior of a coaxial injector that generates highly monodispersed emulsion in a jetting mode over a wide range of bubble sizes. The ranges of Weber numbers and Reynolds numbers explored in this experimental investigation were extremely small, as will be discussed later, so that inertia played a negligible role in the observations reported. In its spirit, the proposed configuration is quite close to the one already proposed by Garstecki *et al.*,[13] for which the injection is performed in a long narrow orifice. In such experimental conditions, where the injector is long and narrow, the so-called jetting regime is no longer irregular or random. On the contrary, it shows a very well-defined, reproducible behavior. This is why we will call this regime a jetting-bubbling regime in what follows. One of our claims in the subsequent analysis is that, contrary to what has been previously proposed in open coaxial flow configurations, this jetting-bubbling regime is not the consequence of a flow instability, but results from a finite-time viscosity dominated

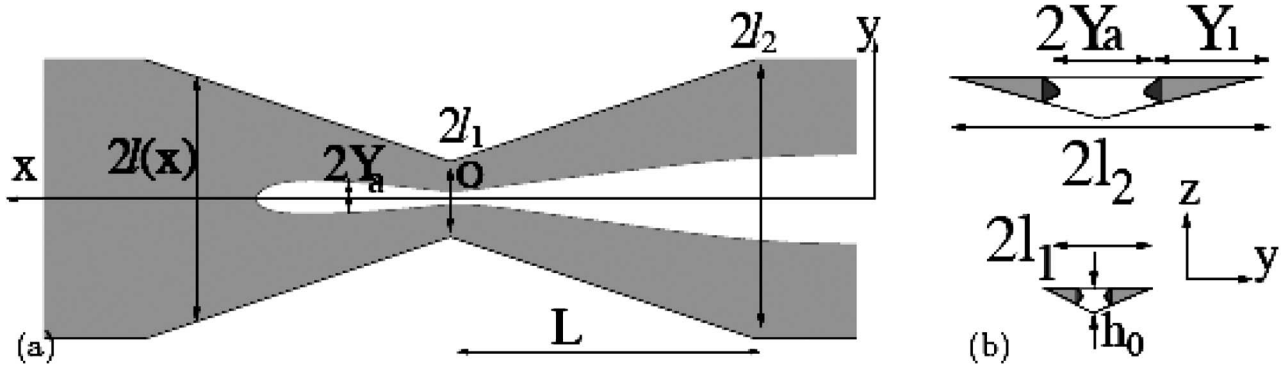

FIG. 1. Schematic representation of the experimental pinched channel. The *perfectly wetting* liquid filling the channel is represented in gray. White indicates the air bubble. (a) (x,y) top view. (b, top) (y,z) channel profiles at $x=-L$. (b, bottom) (y,z) channel profiles at $x=0$.

and geometrically controlled pinching. One of the important advantages of our configuration compared to previous ones is the possibility of deriving lubrication arguments that provide a description of the interface scaling dynamics that is consistent with experimental observations.

The sensitivity of bubble generation to the flow properties as well as the bubbling dynamics is studied. We present experimental evidence that a pinched channel can be used as a very sensitive flow-meter and/or encapsulation injector. It is found that the bubbling frequency and the bubble size generated by such a device are sensitive to the injected flow rate over several decades, leading to bubble sizes that can vary by a factor 4 in the range of parameters analyzed in this paper. Very small flow rates can then be continuously measured by the device, the range of which could be easily adjusted by means of the channel geometry.

II. EXPERIMENTS

Many techniques have recently been developed to fabricate complicated geometries, among which micromachining is an interesting and ubiquitous one.[15] Using this technique, a "pinched channel" (cf. Fig. 1) was carved in epoxy resin and covered with a PDMS plate. The purpose of this study was to investigate how a geometrically pinched channel, like the one represented in Fig. 1, could affect the dynamics of a confined coflowing gas liquid. The resulting aperture $h(x,y)$ between the two surfaces in the vicinity of the origin taken to be at O, whose (x,y) position was thus $(0,0)$, had linear spatial variations in both the x and y directions,

$$h(x,y) = h_0\left(1 + \frac{\Delta\ell}{L}\frac{|x|}{\ell_1} - \frac{|y|}{\ell_1}\right) \quad \text{for } |x| < L, \tag{1}$$

where $h_0=0.25$ mm is the vertical gap at the constriction origin point O located at $(x=0,y=0)$, $\Delta\ell=\ell_2-\ell_1$, while $\ell_1=5$ mm and $\ell_2=20$ mm are its half-width at $x=0$ and $x=L=90$ mm, respectively. The channel half-width $\ell(x)$ is defined implicitly from the relation $h(x,\ell(x))=0$, so from (1), it found to be equal to $\ell(x)=\ell_1+\Delta\ell|x|/L$ for $|x|<L$. Moreover, since the air and liquid fill the whole channel, the air and liquid half-widths $Y_{a,l}$ depicted in Fig. 1(b) are simply related to the channel half-width by $\ell=Y_a+Y_l$.

For $|x|>L$, the channel profile and width are longitudinally invariant and equal to their value at $x=\pm L$, i.e., $h(\pm L,y)=h_0(\ell_2-|y|)/\ell_1$ and $\ell(x=\pm L)=\ell_2$. It should be borne in mind that, because the observed phenomena only depend on suitable dimensionless parameters, all these geometrical parameters are illustrative, and proper downscaling can be deduced from the analysis presented. The values of the geometrical parameters of the channel were chosen for two main reasons. First, we sought to study a "squashed" channel for which the gas-liquid interface could be easily visualized by direct optical inspection. So the channel dimensions in the z direction were much smaller than in x and y as depicted in Fig. 1(b), and as already analyzed in Ref. 17. Furthermore, since we were also interested in a theoretical understanding of this question, we kept small slopes everywhere in the channel's spatial variations, so that lubrication arguments could be used. For simplicity, both y and z variations were taken to have the same slope of 5%, which then fixed the length L. Finally, the dimension h_0 was chosen much smaller than the capillary length, which was close to 2 mm in our case. Hence, the Bond number was very small (less than 10^{-2}) and the influence of gravity will not be considered here. The wetting properties of the silicon oils on the epoxy resin in which the pinched channel was carved were measured by an optical method. The wetting angles were always found to be smaller than the uncertainty of the measurement, which was 5 degrees. The same conclusions were obtained for the wetting angle of the silicon oils on the top Plexiglas plate. So the channel solid surfaces will be considered as uniformly perfectly wetted by the silicon oil. Because of the large viscosity ratio between the gas and the liquid, the pressure variations were essentially localized in the liquid, while the gas pressure was almost uniform. Hence, within the considered limit of very small Reynolds number flow (this statement will be further investigated later on), pushing the gas or pulling out the liquid was essentially the same problem. One side of the channel was open to ambient pressure while the other side was connected to a screw-driven pump through a Plexiglas injector. Experiments were carried out by slowly pumping out the perfectly wetting silicon oil while recording the liquid-gas interface temporal variation above the channel with a CCD camera using wide angle

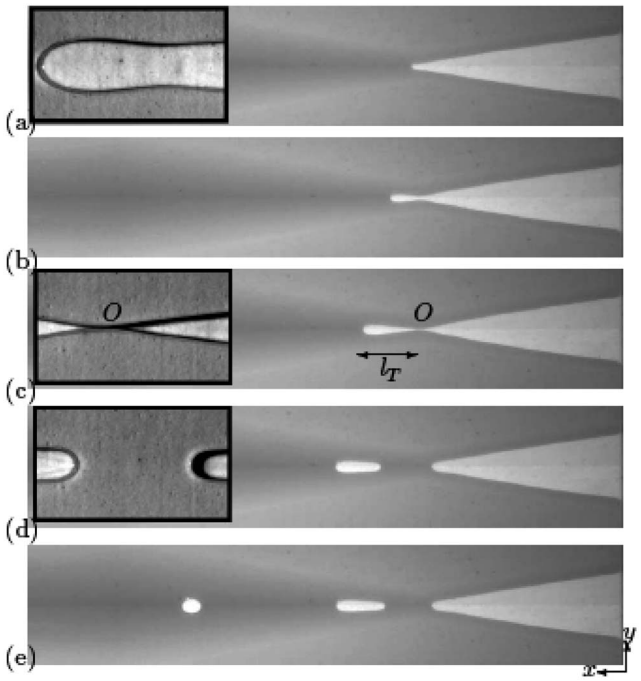

FIG. 2. Experiment. Top view of the liquid (in gray) and gas (in white) flows inside the channel at different times, increasing from (a) to (e). (a) Just after crossing the pinched point O. (b) Growth of a slowly pinched bubble. (c) Just before pinching occurs, with $\ell_T \simeq 20$ mm here. (d) Just after pinching. (e) One time period after (d). Insets in (a), (c), and (d) display a 10 mm$\times$5 mm zoom of the bubble interface in the vicinity of the pinched point.

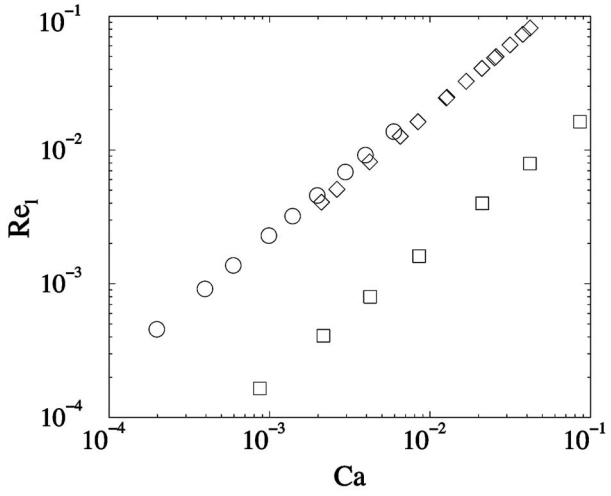

FIG. 3. Reynolds number versus Capillary number in log-log coordinates.

optics. When the gas phase (air) was injected at a constant flow-rate into the microchannel depicted in Fig. 1(a), previously filled up with silicon oil, the bubble formation was found to be highly reproducible. After entering the constriction [see Fig. 2(a)], the interface started to slowly change shape so as to form a long finger with concave curvature at the constriction point O [see Fig. 2(b)]. This finger had a large aspect ratio and deformed slowly as its nose was pushed forward. In the meantime, the finger interface tail in the vicinity of the constriction point O shrank because of the capillary pressure gradient. At a given time $t=0$, the interface [see Fig. 2(c)] reached a limit after which very fast capillary pinching occurred at the constriction point O. The bubble length l_T was maximal at this instant, then rapidly decreased, as can be seen in Figs. 2(d) and 2(e). After a period T, the phenomenon reoccurred with a well-defined frequency, having relative variations (the ratio of standard deviation to the mean) smaller than 5%. This well-defined bubbling period could nevertheless be perturbed at large flow rates and high frequencies when formation of one bubble was perturbed by the preceding one. Moreover, the experiments were carried out in an environment where the temperature was controlled at 21 °C with relative variation smaller than 0.5 °C. The silicon oil viscosity and surface tension variations caused by a 2 °C variation around this room temperature were close to 20% and 10%, respectively. A three-degree difference in temperature was enough to produce frequency variations as large as 30%. Hence, the bubbling frequency is extremely sensitive to temperature or viscosity variations, and this sensitivity could be of interest for future applications. Nevertheless, most of the experiments were carried out with temperature controlled so closely that only 10% variations of the frequency were observed in most cases. Moreover, the experimental estimation of the observed frequency could be made very precise, by averaging over a large number of events. Three silicon oils with dynamic viscosities μ equal to 0.019, 0.068, and 0.22 Pa s were used while varying the volume flux from 2.77×10^{-4} to 1.38×10^{-2} ml s^{-1}. Their silicon oil/air surface tensions γ, measured with a Langmuir-Wilhelmy balance, were 20.7, 21.7, and 23.3 mN m^{-1}, respectively. The relevance of inertia effects in our experiments was investigated through the evaluation of the Reynolds number Re_l, which, in this slow, quasistationary dynamical regime of lubrication flows, can be written $\mathrm{Re}_l = (\Delta\ell/L)h_0\rho(Q/\ell_1 h_0)/\mu$, where ρ is the fluid density of the silicon oils used, which were found so similar that they could all be taken as equal to $\rho=968$ kg m^{-3}. The variation of this number is plotted in Fig. 3 versus the Capillary numbers associated with the Fig. 4 experiments.

It can be observed that this number is indeed extremely small, which confirms the fact that inertial effects did not play a role in the configuration considered.

Let us now examine the relation between the bubbling frequency and the flow rate. Figure 4(a) represents the bubbling frequency $1/T$ (averaged over 30 events), as a function of the gas flow rate Q. It can be seen, as expected, that the frequency increases with the imposed flux. However, the observed relation is not linear and depends on the fluid properties. When this frequency is nondimensionalized with the capillary-viscous time $t_{\mathrm{cv}}=(\ell_1/h_0)^{3/2}(L/\Delta\ell)\mu\ell_1/\gamma$ plotted versus the Capillary number $\mathrm{Ca}=\mu Q/h_0\ell_1\gamma$, all the experimental points fall nicely along a single curve, Fig. 4(b). It should be noted that this Capillary number differs from the usual one defined with the averaged fluid velocity by a factor 4/3 that has been included in the forthcoming analysis. It can be seen in Fig. 4(b) that the nondimensionalized frequency varies over more than two decades with similar variations for the Capillary number. A power-law relation between the fluid

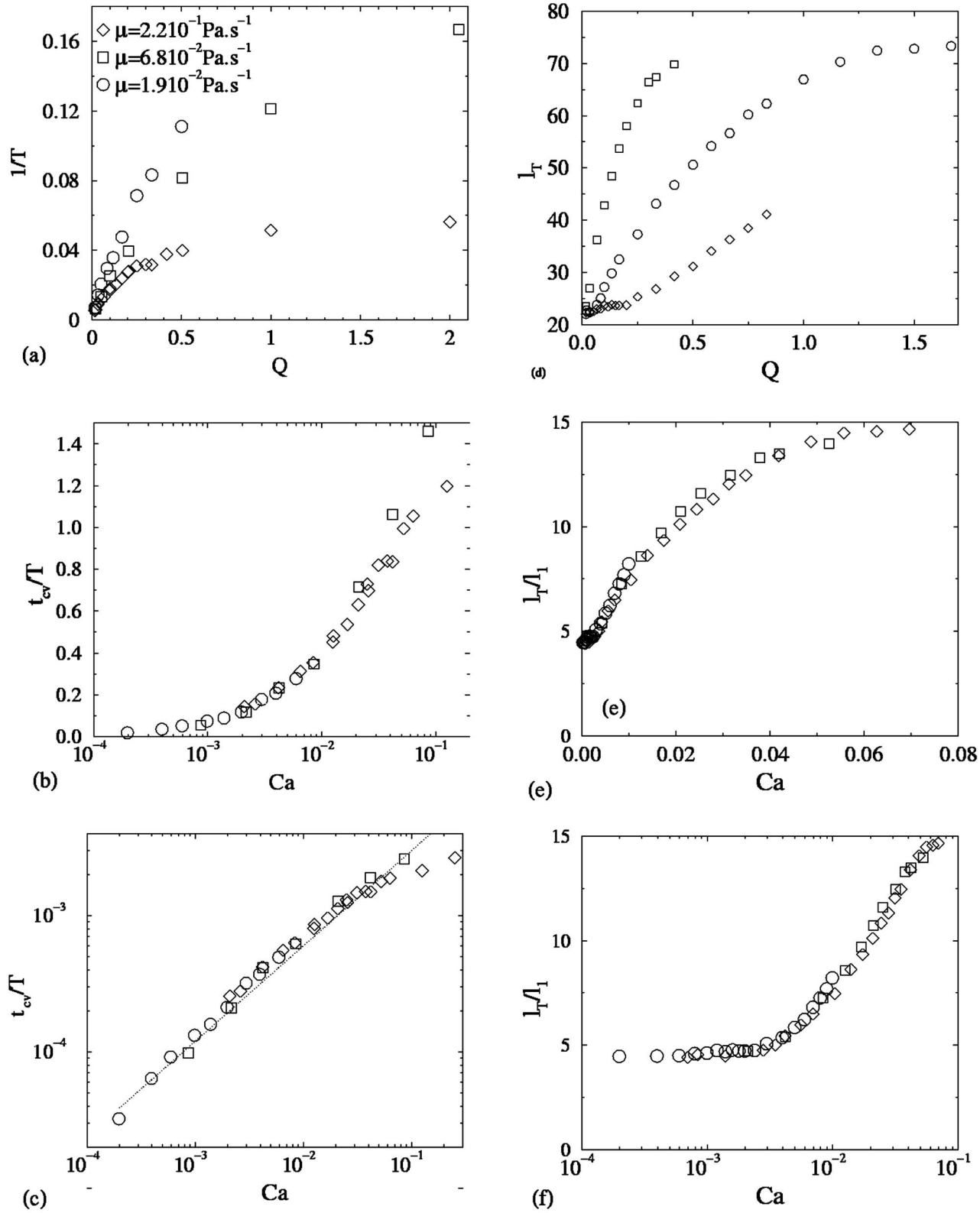

FIG. 4. (a) Bubbling frequency $1/T$ in Hertz as a function the imposed flux Q in ml min^{-1} for silicon oils having three different dynamic viscosities μ. (b) Bubbling frequency nondimensionalized by the capillary relaxation time $t_{cv}=(\ell_1/h_0)^{3/2}(L/\Delta\ell)\mu\ell_1/\gamma$ versus the Capillary number $\mathrm{Ca}=\mu Q/l_1h_0\gamma$. The capillary variations are displayed on a logarithmic scale. (c) log-log plot of data represented in (b) where the continuous line has a slope of 0.7. (d) Bubble length l_T represented in Fig. 2(c) in millimeter versus the imposed flux Q in ml min^{-1} for silicon oils having three different dynamic viscosities μ. (e) Nondimensionalized bubble length versus the Capillary number. (f) Same data as in (e) with capillary variations displayed on a logarithmic scale.

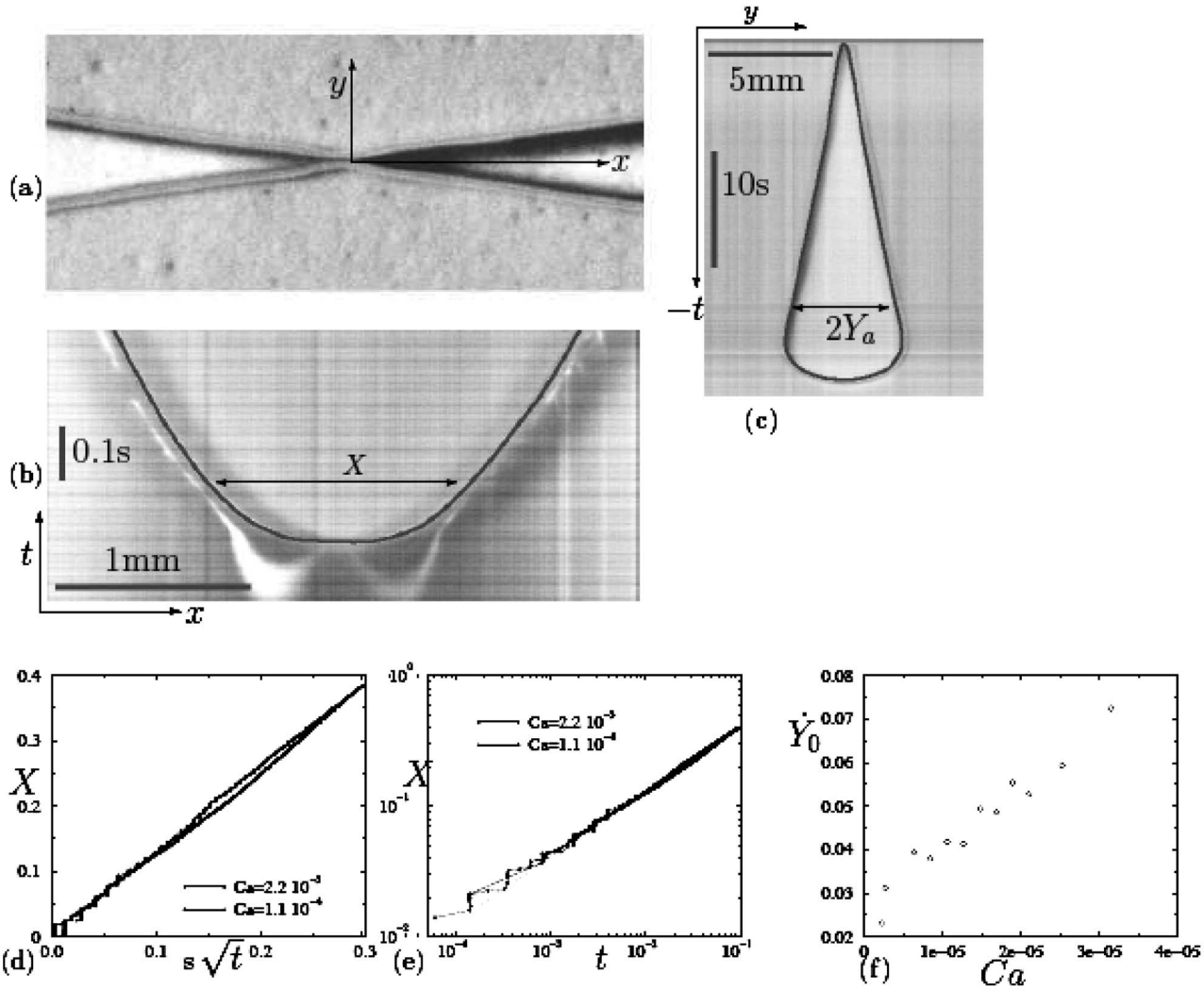

FIG. 5. Spatio-temporal behavior of the observed liquid-air interface (represented with a black line) near the origin O before and after pinching. (a) Image of the liquid-air interface at the origin O at pinching taken as the reference time $t=0$. One transverse line along y and one horizontal line along x were chosen to study the temporal behavior. (b) Spatio-temporal diagram extract along the x axis displayed in (a) after pinching. (c) Spatio-temporal diagram along the y axis displayed in (a) before pinching. (d) Spatial separation X (in millimeters) displayed in (b) between the two post-pinch recoils versus $\sqrt{t}$ (in seconds). (e) Same data as in (d) represented in log-log coordinates. The dotted line has a slope of 1/2. (f) Vertical velocity of the fluid at the saddle point $\dot{Y}_0=\dot{Y}_l(x=0,t)$ versus the Capillary number.

flux and the Capillary number can be deduced from the observed data, so that the experimental observations can be recast in a simple scaling relation $\mu\ell_1/\gamma T \sim \mathrm{Ca}^{\nu}$, where the exponent ν was estimated experimentally as close to $\nu \simeq 0.7$. This illustrates the fine-tuning of the bubbling frequency over a wide range of fluxes. The same collapse is observed on the bubble length l_T with the Capillary number. It is interesting to note that the bubble length saturates at a minimum value close to $\ell_{Tc} \simeq 4.5\ell_1$ as the Capillary number decreases. This saturation of the bubble length with the imposed flux is what we will refer to as the transition between the dripping regime and the jet regime. This saturation is expected at a quasistatic small capillary limit where the capillary pressure gradient becomes predominant over the viscous pressure gradient. In the following, we will develop some theoretical arguments to find the critical Capillary number associated with the transition between these two regimes. Hence in the dripping regime, the air bubble is produced at the entrance of the channel, and the size is mainly controlled by the channel width because it is directly related to the capillary pressure independently of the imposed flow. In contrast, in the jet regime, the bubble length increases with the imposed flux, and can become 20 times larger than the channel width.

Let us now discuss the main characteristics of the fast dynamic regime. In order to investigate this regime, we used a fast camera to record a small region of the channel in the vicinity of the pinched point O at a frequency of about 300 images per second. We investigated the dynamic behavior of the liquid-gas interface just after the pinch. In Fig. 5, the pinch is taken as the origin of time and space. Negative times are associated with the slow dynamics considered above. Positive times are associated with the fast interface dynamics just after the breakup. As illustrated in Figs. 5(b), 5(d), and 5(e), the interface longitudinal distance X shows a very fast longitudinal displacement that varies linearly with the square

root of time. This behavior is very weakly dependent on the imposed liquid flux or other experimental conditions, as illustrated in Figs. 5(d) and 5(e). This behavior is quite distinct from the slow dynamics associated with bubble growth.

III. THEORETICAL ANALYSIS

In this section, we analyze the main features of the experiments described in the previous one. First, in Sec. III A, we present some important considerations related to confined two-phase flows at small Capillary numbers. Then we discuss the relevant length scales of the problem, and the nondimensionalization. Using these elements in Sec. III B, we analyze the critical Capillary number for the transition between the dropping and the jetting regimes. Furthermore, we analyze the bubbling frequency from a scaling argument associated with the slow dynamics of the bubble formation. Finally, we describe some features of the fast dynamics of the bubble.

A. Lubrication analysis

Let us first discuss the relative length scales associated with our channel. By examining the gap chosen in (1), we note that the channel length is larger than its width, which is larger than its height. There is thus a hierarchy of length-scale variations that follows $\partial_z \gg \partial_y \gg \partial_x$. To be more precise, the typical dimensions associated with the z and y coordinates are the channel's width and height at the pinched point so that $z \sim h_0$ and $y \sim \ell_1$. This is still true near the pinch point O, even though the bubble half-width Y_a tends to zero at time $t=0$, since the scales considered are associated with the liquid film half-width, as already discussed in Sec. II. From the definition of the gap (1), it is easy to find that transverse and longitudinal variations are related to the longitudinal one such that $x \sim \ell_1 L/\Delta\ell$. From this, one finds that $\partial_y \sim O(h_0/\ell_1)\partial_z$, while $\partial_x \sim O(\Delta\ell/L)\partial_y$. Using the experimental data $h_0/\ell_1 \simeq 0.05$ and $\Delta\ell/L \simeq 0.16$, a quantitative estimate of these relative orders can be obtained. Thus, it is now important to realize that, to leading order, most of the physics associated with two-phase flow in Hele-Shaw cells can be transposed to our problem because of this length-scale decoupling. Nevertheless, we will not proceed to a systematic asymptotic derivation of the hydrodynamics, for it is a heavy task that would go well beyond the scope of this paper, and much of it would not draw new material out of previous studies such as Refs. 18–21. We will restrict ourselves to writing the leading-order dynamical equations, the scaling of which will be analyzed in comparison with the experimental data presented in the previous section. Since the x and y variations are smaller than the z ones, the leading-order problem for the interface displacement is associated with two-phase flow in a Hele-Shaw cell, as depicted in Fig. 6. We then consider the hydrodynamics associated with the slow flow regime, for which the air bubble gently displaces the fluid. Let us first consider the liquid around the air bubble. Because the viscosity ratio between the air and the liquid is very large (larger than 10^{-4}), the shear stress induced in the gas by the liquid flow is very small. Hence, the flow in the gas is very weak, and the pressure drop associated with the

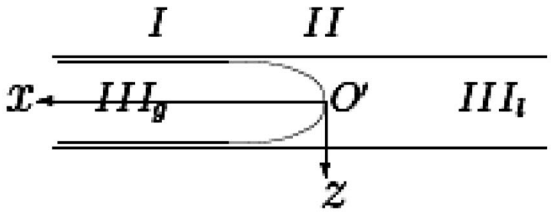

FIG. 6. Lateral view of the bubble shape in the (O',x,z) plane. The origin of coordinates is taken at the bubble tip O'.

gas flow is completely negligible compared with that associated with the liquid flow. The normal-stress equilibrium is thus compensated by the capillary pressure, so that the interface shape of the bubble adapts its curvature to maintain a constant pressure in the gas. In the following, we take the gas pressure as a reference pressure equal to zero, and consider the liquid pressure denoted P. Numerous previous studies have considered viscous fluid flows in confined channels, within the limit of small Capillary numbers. Within this limit, under perfectly wetting conditions, the gas-liquid interface confined between two solid surfaces displays three distinct regions. A constant thin-film region in the vicinity of solid surfaces (region I, Fig. 6), a meniscus region associated with the liquid-gas interface (region II, Fig. 6), and the clear original wetting fluid region (region III_l, Fig. 6). These three regions are associated with different dominant forces.[22] In region I, viscosity forces are dominant, because the curvature of the interface becomes equal to zero. In region II, capillary forces associated with the liquid-gas surface tension γ are dominant: the liquid-gas interface has a quasistatic quadratic shape that is locally controlled by the perfectly wetting boundary conditions at the solid surface. In the third region III_l, the fluid flow is again dominated by viscosity, so that the liquid flow field has a simple local parabolic profile. The identification of these regions and their related dominant forces have provided the correct scaling for the characteristic dimensions, flow, and pressure.[18,22] When the viscosity ratio between the gas and the liquid is considered negligible, the scaling is given using a single dimensionless small parameter: the Capillary number Ca. The perturbation expansion in this small parameter of this problem is known to be singular, so matched expansion techniques are needed to relate the interface curvature in the static meniscus region II to the thin-film region I. Hence, it is possible to find the pressure difference between regions I and III as a function of the geometry and Capillary number. As discussed in Ref. 17, the class of narrow channel that is considered in this study is such that the lateral and longitudinal variations are slow. In this context, the conclusions reached by different contributors such as Park and Homsy,[18] Reinelt,[19,20] and Burgess[21] on the liquid pressure P apply to our problem, and the liquid pressure is asymptotically equal to

$$P = -\left[\frac{2\gamma}{h} + \frac{\pi\gamma}{4R} + \mathrm{Ca}_n^{2/3}\left(\frac{7.6\gamma}{h} + \frac{4.07\gamma}{R}\right)\left(\frac{4}{3}\right)^{2/3}\right], \qquad (2)$$

where the vertical gap h defined in (1) should be evaluated at position $h(x,Y_a)$, where $Y_a(x,t)$ stands for the gas-liquid in-

terface half-width and Ca_n is the Capillary number associated with the velocity normal to the gas-liquid interface, i.e., $\mathrm{Ca}_n=\mathrm{Ca}\partial_x Y_a/\sqrt{1+\partial_x Y_a^2}$. The first and second terms on the right-hand side (r.h.s.) of (2) are the static capillary pressure coming from the Laplace law when the zero reference pressure in the gas is chosen. Since the fluid interface is locally semicircular in the gap, the first principal curvature is related to the local vertical aperture h given in (1), while the (x,y) plane curvature is $1/R(x,t)=-\partial_x^2 Y_a(1+\partial_x Y_a^2)^{-2/3}$. The third and fourth terms on the r.h.s. of (2) come from the viscous contribution of thin-film displacements near the channel top and bottom walls[17] while other viscous contributions in the channel gap are O(Ca). It is worth noting that this asymptotic liquid pressure in region III_l depends neither on the vertical position z nor on the transverse coordinate y, but only on the longitudinal position x of the interface located at transverse position $Y_a(x,t)$.

In order to derive the dynamic equation for the interface, one has to self-consistently consider the momentum equations, fluid incompressibility, and kinematic boundary conditions. The momentum equations associated with the fluid flow are the Stokes equations since we are considering the creeping flow limit associated with zero Reynolds number. Following conventional derivations of the lubrication approximation, those equations degenerate into the Reynolds equations relating the local pressure longitudinal variations with the leading-order longitudinal component u of the velocity field $\mathbf{u}=(u,v,w)$,[23,24]

$$u=-\frac{z[z-h(x,y)]}{2\mu}\partial_x P, \tag{3}$$

where μ is the liquid dynamic viscosity. From this Reynolds equation, it is easy to find the longitudinal component q_x of the flux, $\mathbf{q}=(q_x,q_y)=\int_0^h(u,v)dz$,

$$q_x(x,y)=-\frac{h^3(x,y)}{12\mu}\partial_x P. \tag{4}$$

The incompressibility of the fluid can be integrated along the z direction, so, by using the no-slip boundary conditions of the w component of the velocity field $\mathbf{u}=(u,v,w)$, we can write the incompressibility condition associated with the flux $\mathbf{q}=(q_x,q_y)$,

$$\partial_x q_x+\partial_y q_y=0. \tag{5}$$

Finally, as usual in Hele-Shaw problems,[25] we use an averaged kinematic boundary condition associated with the averaged components of the velocity field with gap-averaged velocity $(\bar{u},\bar{v})=(\int_0^h u dz/h=q_x/h,\int_0^h v dz/h=q_y/h)$. We define the interface position associated with the implicit condition on F_p,

$$F_p(x,y,t)=y-Y_a(x,t)=y-\ell(x)+Y_l(x,t)=0, \tag{6}$$

where we have used the liquid half-width definition $Y_l=\ell-Y_a$ as depicted in Fig. 1(b). The kinematic boundary condition is then easily obtained by imposing a zero Lagrangian derivative on $F_p(x,y,t)$ over the gap-averaged velocity $(\bar{u},\bar{v})$,

$$\frac{DF_p}{Dt}=\partial_t F_p+\bar{u}\partial_x F_p+\bar{v}\partial_y F_p=\partial_t Y_l-\frac{q_x}{h}\partial_x Y_a+\frac{q_y}{h}=0. \tag{7}$$

Since $q_y(x,\ell)=0$, integrating the incompressible condition (5) along the transverse coordinates y from $y=Y_a(x)$ to $y=\ell(x)$, leads to

$$\int_{Y_a}^{\ell}\partial_x q_x-q_y(x,Y_a,t)=0. \tag{8}$$

Since equally $q_x(x,\ell)=0$, one has

$$\partial_x\int_{Y_a}^{\ell}q_x dy=\int_{Y_a}^{\ell}\partial_x q_x dy-\partial_x Y_a q_x(x,Y_a,t). \tag{9}$$

Considering now the kinematic boundary condition (7), the integrated incompressibility condition (8) and relation (9) lead to

$$\partial_x\int_{Y_a}^{\ell}q_x dy=-h(x,\ell-Y_l)\partial_t Y_l. \tag{10}$$

Now, using the gap geometry (1) together with the Reynolds-Darcy relation (4) between the longitudinal flux and the pressure longitudinal gradient, it is easy to perform a simple algebraic integral on the left-hand side of (10) to find the dynamic equation for the liquid half-width associated with the slow bubble growth,

$$Y_l\partial_t Y_l=\frac{h_0^3}{48\mu\ell_1^3}\partial_x(Y_l^4\partial_x P). \tag{11}$$

A similar dynamic equation was derived in Ref. 26 for the dynamic of a liquid film confined in a corner. This governing equation is nonlinear and depends on the longitudinal pressure variations. Let us now discuss the scaling behavior of the resulting flow.

B. Scaling analysis

1. Transition between dropping and jetting-bubbling regimes

In this section, we would like to derive the ratio between capillary pressure and viscous dissipation at the pinched point. This should enable us to find a criterion for the transition between a capillary dominated and a viscosity dominated regime for the bubbling air. From (2) one can see that, within the limit of zero Capillary number, the static equilibrium imposes a constant pressure in the fluid, associated with a constant mean curvature $\kappa=2/h+\pi/4R$ of the interface. This means that, as the bubble grows slowly, the interface is quasistatically displaced so that its mean curvature is kept constant within some small capillary corrections. Since this mean curvature is spatially constant, the first two terms of relation (2) do not contribute to the pressure gradient within the limit of small Capillary numbers, so that the leading-order pressure gradient is associated with the third and fourth viscous dissipation terms. From symmetry considerations, the liquid-gas interface has a quadratic shape in the (x,y) plane in the vicinity of point O. Hence for $t<0$, $\partial_x Y_a(0,t)$

$=0$. Thus, it is possible to find a simple expression for the longitudinal pressure gradient at the pinched point O by deriving Eq. (2) along the longitudinal direction, to give $\partial_x P(0,t)=(\gamma/h_0)c\mathrm{Ca}^{\frac{2}{3}}\partial_x^2 Y_a(0,t)$, where constant $c=(-3.34+6.26\kappa h_0)$. We still need to evaluate the second derivative of the interface at the pinched point O. By using $\partial_x Y_a(0,t)=0$ again, it is possible to find a simple relation between this second derivative and the mean-plane curvature at the pinched point, $\partial_x^2 Y_a(0,t)=1/R(0,t)$. Now, considering that longitudinal variations in (1) are $O(\Delta\ell/L)$ smaller than transverse ones, it is possible to use a result previously obtained in Ref. 17 for a channel having no longitudinal width variations. It is indeed found in Ref. 17 that an asymptotic expression for the quasistatic mean curvature of the liquid-gas interface can be obtained as a function of the channel aspect ratio h_0/ℓ_1,

$$\kappa h_0 = 2 + \sqrt{\frac{\pi h_0}{\ell_1}}. \tag{12}$$

This result was obtained by neglecting $O(h_0/\ell_1)$ terms, but will be completed by omitting $O(\Delta\ell/L)$ terms in our context. Using $\partial_x^2 Y_a(0,t)=1/R(0)=(4/\pi h_0)(\kappa h_0-2)=4(h_0\pi\ell_1)^{-1/2}$, we find the leading-order longitudinal pressure gradient,

$$\partial_x P(0,t) = -(4c\gamma/h_0\sqrt{h_0\pi\ell_1})\mathrm{Ca}^{2/3}. \tag{13}$$

The transition between the dropping and the jetting regimes should occur when this pressure gradient balances the viscous pressure gradient. Let us first evaluate the relation between the viscous pressure gradient and the Capillary number. From the fluid incompressibility, the total liquid flux Q obtained by integrating $q_x(x,y)$ spanwise along the y direction is longitudinally invariant. Moreover, since the boundary conditions are stationary, this total flux is also stationary. Hence, we can evaluate that the total liquid flux Q_c at the pinching limit, at $x=0$, and just before pinching occurs, at $t=0^-$, $Q_c=2\int_0^{\ell_1} q_x(0,y)dy$, which, from (4), (13), and (1) giving $\int_0^{\ell_1} h^3(0,y)=\ell_1 h_0^3/4$, enables us to evaluate the critical Capillary number $\mathrm{Ca}_c=\mu Q_c/\ell_1 h_0\gamma=(c/6)(h_0/\pi\ell_1)^{1/2}\mathrm{Ca}_c^{2/3}$. Using (12) to obtain an explicit expression for constant c, this leads to

$$\mathrm{Ca}_c = \left(\frac{-3.34+6.26(2+\sqrt{\pi h_0/\ell_1})}{6}\right)^3\left(\frac{h_0}{\pi\ell_1}\right)^{3/2}. \tag{14}$$

As expected from its derivation, this critical Capillary number depends only on geometrical parameters. This analysis is similar to the one proposed in Ref. 13, except for the fact that, here, the thin-film Bretherton capillary pressure is balanced by the bulk viscous pressure instead of the static capillary pressure. More remarkably, it only depends on a single parameter, which is the channel aspect ratio at the pinched point h_0/ℓ_1. For the experimental value $h_0/\ell_1=0.05$, the evaluation of (14) gives $\mathrm{Ca}\simeq 8\times 10^{-3}$, which is consistent with the transition observed in Fig. 4(d). For Capillary numbers smaller than this value, the longitudinal pressure gradient is dominated by the capillary forces and the bubble length no longer varies when the fluid flux changes. In contrast, when the viscous pressure gradient, which is order O(Ca), becomes dominant over the capillary one, which is $\mathrm{O(Ca)}^{2/3}$, then the bubble length increases with the applied flux.

2. Scaling analysis of the dynamic regimes

Let us now discuss the dynamic scaling observed in Fig. 4(b). This scaling can be understood by following the lubrication arguments developed in the previous section. Let us first consider slow bubble growth since bubble formation is directly related to this slow dynamic regime, because the rapid pinch-off is faster than one percent of the total bubbling period. Figure 5(c) shows that the slow time scale, T, of the interface has a linear spatio-temporal variation, so that the interface velocity is constant during this regime. A constant velocity of the transverse displacement of the bubble interface at the pinched point O was measured, the variation of which with Ca is shown in Fig. 5(e). From this observation, we can try to identify a typical evolution time T from the nonlinear evolution equation (11). First, one has to realize that the scaling relation (13) obtained for the pressure gradient at the pinched point also holds everywhere along the longitudinal axis, since it is due to the fact that the mean curvature makes no contribution to the longitudinal pressure gradient. Thus, we can find the dependence of the evolution time T by substituting the scaling of (13) on the r.h.s. of (11), while using the scaling previously discussed for longitudinal variations $x\sim\ell_1\Delta\ell/L$,

$$\frac{\mu\ell_1}{\gamma T} \sim \left(\frac{h_0}{\ell_1}\right)^{3/2}\frac{\Delta\ell}{L}\mathrm{Ca}^{2/3}. \tag{15}$$

This 2/3 power scaling with the Capillary number gives a good estimate of the observed experimental exponent $\nu\simeq 0.7$ associated with Fig. 4(b). It should be noted that this scaling is mainly associated with the dripping regime for which the Capillary number is small enough for (13) to be still valid. The experimental measurements can then be nondimensionalized using the capillaro-viscous time scale t_{cv} obtained from (15), i.e., $t_{\mathrm{cv}}=(\ell_1/h_0)^{3/2}(L/\Delta\ell)\mu\ell_1/\gamma$, as represented in Fig. 4(b). They show, surprisingly, that the 2/3 scaling exponent regime applies over a broad range of Capillary numbers, even when the Capillary number exceeds the critical value $\mathrm{Ca}_c\simeq 8\times 10^{-3}$ obtained in (14), where jetting–bubbling occurs. Moreover, comparing the scaling (15) for the dimensionless frequency with the experimental observation indicates that the prefactor is close to 5. Finally, we should also consider the fact that, when the gas bubble is close the pinch point, a Rayleigh instability could be responsible for the capillary pinching. Our derivation only took the dynamics of the basic flow into account, which leads to a pinching of the gas-liquid interface at finite time. Close to the pinch point, the vertical and horizontal dimensions of the gas bubble are of similar size, so that it has a cylindrical shape whose radius is close to $h_0/2$. From classical results associated with the outer fluid capillary destabilizing effect, it can be found that the Rayleigh instability growth rate is $\omega=\gamma h_0/2\mu$. Hence, the ratio between the typical time scale for the instability to develop and those of the basic flow t_{cv} obtained in (15) is $\omega t_{cv}=(\ell_1/h_0)^{5/2}(2L/\Delta\ell)$, which is very

large. Using the experimental values, ones finds that this ratio is close to 2×10^4. Hence the instability time scale is much smaller than that of the basic flow, and the instability is probably responsible for the occurrence of pinching, since any perturbation has plenty of time to grow, as the basic flow changes the shape of the interface. Nevertheless, the time scale associated with the Rayleigh instability is so small compared with that associated with the basic flow, t_{cv}, that it makes a negligible contribution to the period of the bubble formation. Most of the time taken for the bubble to grow is associated with the gentle viscous deformation of the interface in the basic flow, rather than the time for the Rayleigh instability to develop. This estimate is also consistent with experimental observations that the pinching location is always very close to the geometrical pinched point O. In fact, the perturbation in the pinching location associated with the Rayleigh instability will be proportional to $U/\omega=3h_0\mathrm{Ca}/2$, where U is the mean flow. Since our Capillary numbers were always smaller than 0.07, the fluctuations in the interface pinching position will, in the worst case, be ten times smaller than the aperture $h_0=0.25$ mm at the pinched point O, i.e., 25 micrometers. A further consequence of this observation is thus that the bubble length ℓ_T is not controlled by the Rayleigh instability but rather by the basic flow, since the perturbation in the bubble size coming from the Rayleigh instability is extremely small. It is precisely a specificity of our pinched channel that the jetting-bubbling regime is not controlled by a capillary Rayleigh instability but rather by the geometrical dimensions of the channel, as already observed in Ref. 13. Finally, it is interesting to mention that, as the gas flow increases, the bubble length also levels up, but there is a maximum value for the bubble length when the bubble tip reaches the open end of the channel. Hence, there is obviously an upper cutoff in the bubble length due to the finite longitudinal size of the channel.

Let us now discuss the main characteristics of the fast dynamic regime. We recall that the interface dynamics is symmetrical across the channel pinched-point origin O, as can be observed in Fig. 5(b). This figure illustrates the very fast recoil of the interface for which the typical time scale is of the order of 50 ms. The parabolic shape of the observed spatio-temporal diagram 5(b) indicates that the distance between the two interface tips increases as the square root of time, as previously discussed at the end of Sec. II. This scaling can again be understood with a crude lubrication argument. First, one should consider the possible impact of inertial effects in this fast regime, by estimating the associated Reynolds number Re_l. By considering that the interface dynamics governs the flow nonstationarity in this regime, the influence of inertial effect now needs to be evaluated by balancing the velocity time variations against the viscous term. We can then evaluate the associated Reynolds number as $\mathrm{Re}_l=X^2/t\nu$, where $X(t)$ and t are the interface position at time t, depicted in Fig. 5(b). One interest of this Reynolds number is that it is almost uniform over the whole fast regime, as opposed to the one previously considered, which would change by a large amount, because the fluid velocity varies considerably with time during the fast regime. From the experimental measurements displayed in Fig. 5(d), we can estimate this number to be of the order $\mathrm{Re}_l=0.2$. Thus, although the interface velocity may be high during the rapid relaxation of the interface, inertial effects are indeed small. Hence, many of the considerations stated in Sec. III A to establish the lubrication approximation of the slow regime can also be applied here. More specifically, the Reynolds equations (3) and (4) that relate the longitudinal pressure gradient to the velocity and the flux in the creeping flow limit still apply. Furthermore, since the Capillary number is still small, the liquid pressure expression (2) is also valid in this regime. In this configuration, the mean curvature of the interface is no longer spatially uniform, so that the leading-order dominant contribution to the pressure gradient comes from the two first terms on the r.h.s. of (2). In fact, from symmetry considerations, it turns out that only the second term makes a contribution to the pressure gradient. The symmetrical shape of the spatio-temporal diagram shown in Fig. 5(a) suggests that the interface dynamics is also symmetrical with respect to the pinch-point origin O. So this is also the case for the liquid pressure. Hence, in the following, we will only consider the pressure difference ΔP between the pinched point O and the liquid-gas interface tip along the x direction, at the recoil tip located at longitudinal position $[x=\pm X(t)/2, y=0]$. From symmetry again, after the breakup, the pinched point O is a stagnation point of the liquid flow.

The main point here is to realize that, at the pinching at $t=0$, a topological transition suddenly arises, for which the interface curvature in the (x,y) plane changes its sign, from being finite and negative at $t=0^-$ to a finite positive value at $t=0^+$. At $t=0^-$, and position $(x=0, y=\pm h_0/2)$, the first term in the static liquid pressure associated with the vertical curvature in (2) is $-2\gamma/h_0$, while the second term is positive, equal to γ/R_0, where R_0 is the (x,y) plane radius of curvature of the interface at the origin at $t=0^-$. At $t=0^+$, and position $(x=\pm h_0/2, y=0)$, the first term in the liquid pressure is still $-2\gamma/h_0$, while the second term is negative, and from (12) it is indeed equal to $-\sqrt{\pi/\ell_1 h_0}$. Hence, after the pinch-off, in the vicinity of the pinched point O, the pressure field has a spatial quadratic structure, which is specific to flow near a stagnation point. The pressure at both finger tips located at $(x=\pm h_0/2, y=0)$ is equal, and lower than that at points $(x=0, y=\pm h_0/2)$. This mechanism explains the sudden recoil, the dynamics of which can be understood from lubrication arguments. The pressure drop ΔP between the origin and the longitudinal position $[x=\pm X(t)/2, y=0]$, $\Delta P=P(0,0)-P[X(t)/2,0]=\gamma(1/R_0+\sqrt{\pi/h_0\ell_1})$, neglecting $O(\Delta\ell/L)$ contributions, then drives the fast liquid flow. Using the lubrication approximation (4) again in the liquid to relate the local pressure gradient to the longitudinal mean fluid velocity leads to $\bar{u}(\pm X/2,t)=\pm dX/dt=\pm h_0^2\Delta P/12\mu X$ neglecting $O(\Delta\ell/L)$ terms. This leads to an interface time variation,

$$X(t)\simeq\left(\frac{h_0^2\Delta P t}{6\mu}\right)^{1/2}, \tag{16}$$

which is consistent with the experimental variations represented in Figs. 5(d) and 5(e).

IV. CONCLUSION

We have studied the response of a micro-injector coflow device that produces sensitive and reproducible periodic microbubbling from a steady-state input flow. This device is composed of a simple pinched channel having different characteristic length scales in different directions. The experimental analysis has shown that the bubbling is sensitive to the flow rate, and presents two main regimes: dripping and jetting. Both regimes lead to very reproducible dynamic characteristics, the sensitivity of which has been investigated by varying the fluid and the flow properties. The use of proper nondimensional parameters has permitted the experimental observations to be recast in two main master curves. Furthermore, the main dynamic characteristics of the observed capillary pinching have been analyzed in the context of a lubrication approximation. A simple theoretical dynamic equation for the slow dynamics has been derived, the scaling analysis of which is consistent with the experimental observations. Similarly, the scaling of the fast recoil dynamics is also consistent with lubrication arguments. Rayleigh instability plays a negligible role in this geometrically driven capillary pinching. This conclusion is noticeably similar to previous ones,[13] but the mechanism responsible for the slow dynamics differs in our case, since the static pressure plays no role because the longitudinal liquid pressure gradient is controlled by the Bretherton viscous contributions. Finally, we think that the specific fast/slow regimes of the dynamics and the very good experimental reproducibility of the phenomenon are remarkable and should be of interest for future investigations.

ACKNOWLEDGMENTS

We thank Marc Prat and Professor Oliver E. Jensen for interesting discussions, D. Anne-Archard for help with the viscosity measurements, and Grégory Dhoye, Sébastien Cazin, and François Esteban for technical support. This work was supported by GDR 2345 "Etanchéité statique par joints métalliques en conditions extrêmes" encouraged by CNES, Snecma-Moteur, EDF, and CNRS.

[1] J. R. Lister and H. A. Stone, "Capillary breakup of viscous thread surrounded by another viscous fluid," Phys. Fluids **10**, 2758 (1998).
[2] J. Eggers, "Non-linear dynamics and breakup of free-surface flows," Rev. Mod. Phys. **69**, 865 (1997).
[3] W. W. Zhang and J. R. Lister, "Similarity solutions for capillary pinch-off in fluids of differing viscosity," Phys. Rev. Lett. **83**, 1151 (1999).
[4] A. Sevilla, J. M. Gordillo, and C. Martinez-Bazán, "Transition from bubbling to jetting in a coaxial air-water jet," Phys. Fluids **17**, 018105 (2005).
[5] H. A. Stone, A. D. Stroock, and A. Ajdari, "Engineering flows in small devices: Microfluidics towards a lab-on-a-chip," Annu. Rev. Fluid Mech. **36**, 381 (2004).
[6] A. M. Gañán-Calvo, M. A. Herrada, and P. Garstecki, "Bubbling in unbounded coflowing liquids," Phys. Rev. Lett. **96**, 124504 (2006).
[7] A. M. Gañán-Calvo and J. M. Gordillo, "Perfectly monodisperse microbubbling by capillary flow focusing," Phys. Rev. Lett. **87**, 274501 (2001).
[8] A. M. Gañán-Calvo, "Perfectly monodisperse microbubbling by capillary flow focusing: An alternate physical description and universal scaling," Phys. Rev. E **69**, 027301 (2004).
[9] T. Cubaud and C. M. Ho, "Transport of bubbles in square microchannels," Phys. Fluids **16**, 4575 (2004).
[10] D. R. Link, S. L. Anna, D. A. Weitz, and H. A. Stone, "Geometrically mediated breakup of drops in microfluidic devices," Phys. Rev. Lett. **92**, 054503 (2004).
[11] A. M. Gañán-Calvo, "Generation of steady liquid microthreads and micron-sized monodisperse sprays in gas streams," Phys. Rev. Lett. **80**, 285 (1998).
[12] P. Garstecki, M. J. Fuerstman, and G. M. Whitesides, "Nonlinear dynamics of a flow-focussing bubble generator: An inverted dripping faucet," Phys. Rev. Lett. **94**, 234502 (2005).
[13] P. Garstecki, H. A. Stone, and G. M. Whitesides, "Mechanism for flow-rate controlled breakup in confined geometries: A route to monodisperse emulsions," Phys. Rev. Lett. **94**, 164501 (2005).
[14] A. S. Utada, E. Lorenceau, D. R. Link, P. D. Kaplan, H. A. Stone, and D. A. Weitz, "Monodisperse double emulsions generated from a microcapillary device," Science **308**, 537 (2005).
[15] S. Sugiura, M. Nakajima, S. Iwamoto, and M. Seki, "Interfacial tension driven monodispersed droplet formation from microfabricated channel array," Langmuir **17**, 5562 (2001).
[16] Y. Dimakopoulos and J. Tsamopoulos, "Transient displacement of a Newtonian fluid by air in straight or suddenly constricted tubes," Phys. Fluids **15**, 1973 (2003).
[17] S. Geoffroy, F. Plouraboué, O. Amyot, and M. Prat, "Quasi-static liquid-air drainage in narrow channels with variations in the gap," J. Colloid Interface Sci. **294**, 165 (2006).
[18] C. W. Park and G. Homsy, "Two-phase displacement in Hele-Shaw cells—Theory," J. Fluid Mech. **139**, 291 (1984).
[19] D. A. Reinelt, "The effect of the thin film variation on shape finger," Phys. Fluids **30**, 2617 (1987).
[20] D. A. Reinelt, "Interface conditions for two-phase displacement in Hele-Shaw cells," J. Fluid Mech. **183**, 219 (1987).
[21] D. Burgess and M. R. Foster, "Analysis of the boundary-conditions for a Hele-Shaw bubble," Phys. Fluids A **2**, 1105 (1990).
[22] F. P. Bretherton, "The motion of long bubble in tubes," J. Fluid Mech. **10**, 166 (1961).
[23] L. G. Leal, *Laminar Flow and Convective Transport Processes*, Series in Chemical Engineering (Butterworth-Heinemann, Boston, 1992).
[24] F. Plouraboué, S. Geoffroy, and M. Prat, "Conductances between confined rough walls," Phys. Fluids **16**, 615 (2004).
[25] F. Plouraboué and E. J. Hinch, "Kelvin-Helmoltz instability in Hele-Shaw cell," Phys. Fluids **14**, 922 (2002).
[26] M. M. Weislogel and S. Lichter, "Capillary flow in an interior corner," J. Fluid Mech. **373**, 349 (1998).